

# Elucidating the Origins of Subgap Tail States and Open-Circuit Voltage in Methylammonium Lead Triiodide Perovskite Solar Cells

Tian Du, Jinhyun Kim, Jonathan Ngiam, Shengda Xu, Piers R. F. Barnes, James R. Durrant,\* and Martyn A. McLachlan\*

Recombination via subgap trap states is considered a limiting factor in the development of organometal halide perovskite solar cells. Here, the impact of active layer crystallinity on the accumulated charge and open-circuit voltage ( $V_{oc}$ ) in solar cells based on methylammonium lead triiodide ( $\text{CH}_3\text{NH}_3\text{PbI}_3$ , MAPI) is demonstrated. It is shown that MAPI crystallinity can be systematically tailored by modulating the stoichiometry of the precursor mix, where small quantities of excess methylammonium iodide (MAI) improve crystallinity, increasing device  $V_{oc}$  by  $\approx 200$  mV. Using in situ differential charging and transient photovoltage measurements, charge density and charge carrier recombination lifetime are determined under operational conditions. Increased  $V_{oc}$  is correlated to improved active layer crystallinity and a reduction in the density of trap states in MAPI. Photoluminescence spectroscopy shows that an increase in trap state density correlates with faster carrier trapping and more nonradiative recombination pathways. Fundamental insights into the origin of  $V_{oc}$  in perovskite photovoltaics are provided and it is demonstrated why highly crystalline perovskite films are paramount for high-performance devices.

## 1. Introduction

The power conversion efficiencies (PCEs) of state-of-the-art solar cells based on organometal halide perovskite solar cells (PSCs) have already exceed 22%,<sup>[1]</sup> such progress is closely associated with improvement of their open-circuit voltage ( $V_{oc}$ ).<sup>[2]</sup> To date, impressive device  $V_{oc}$  values, exceeding 1.2 V, have been achieved for PSCs with an optical bandgap ( $E_g$ ) of 1.6 eV.<sup>[3]</sup> However, the photovoltages demonstrated do not yet reach the radiative efficiency limit.<sup>[4]</sup> Further reducing nonradiative photovoltage loss, either in the bulk active layer or at interfaces within the cell are key strategies to breaking the current efficiency record.<sup>[5]</sup>

Most of the high-efficiency, and therefore high  $V_{oc}$  (>1 V), PSCs are fabricated with the conventional n-i-p structure, normally with planar or planar/mesoporous  $\text{TiO}_2$  as an electron transport layer (ETL)

deposited on a transparent electrode.<sup>[6]</sup> The loss of  $V_{oc}$  has been discussed in terms of interfacial recombination induced by top hole transport layers (HTLs),<sup>[3]</sup> or by bottom ETL.<sup>[7]</sup> Inverted devices, i.e., p-i-n architectures, comprising poly(3,4-ethylene dioxithiophene):polystyrene sulfonate (PEDOT:PSS) as bottom HTLs are associated with greater losses in photovoltage and their  $V_{oc}$  is usually more than 100 mV lower than the  $V_{oc}$  achieved with n-i-p devices.<sup>[8]</sup> Despite these observed performance limitations, such devices are attractive due to their inherent compatibility with low temperature processing and reduced current-voltage ( $J$ - $V$ ) hysteresis,<sup>[9]</sup> which has been associated with low interfacial recombination rates.<sup>[10]</sup> In direct contradiction to this, significant  $V_{oc}$  losses have been attributed to strong recombination at the PEDOT:PSS/perovskite interface, and are shown to be suppressed by surface modification of PEDOT:PSS.<sup>[11]</sup> Higher  $V_{oc}$  values, i.e., >1 V, have been achieved in devices where PEDOT:PSS is replaced with polymeric HTLs,<sup>[12,13]</sup> or p-type metal oxides,<sup>[14]</sup> resulting in PCEs approaching 20%. Similar effects of reducing interfacial recombination to boost  $V_{oc}$  are also observed at perovskite/ETL interface.<sup>[15-17]</sup>


As photogenerated charge carriers are shown to accumulate in the perovskite active layer as well as the contact layers under open-circuit conditions,<sup>[18,19]</sup> nonradiative losses in the bulk

T. Du, J. Ngiam, S. Xu, Dr. M. A. McLachlan  
Department of Materials and Center for Plastic Electronics  
Imperial College London  
SW7 2AZ London, UK  
E-mail: martyn.mclachlan@imperial.ac.uk

T. Du, J. Kim, Prof. J. R. Durrant  
Department of Chemistry and Center for Plastic Electronics  
Imperial College London  
SW7 2AZ London, UK  
E-mail: j.durrant@imperial.ac.uk

Dr. P. R. F. Barnes  
Department of Physics and Center for Plastic Electronics  
Imperial College London  
SW7 2AZ London, UK

Prof. J. R. Durrant  
SPECIFIC IKC  
College of Engineering  
Swansea University  
SA2 7AX Swansea, UK

 The ORCID identification number(s) for the author(s) of this article can be found under <https://doi.org/10.1002/adfm.201801808>.

© 2018 The Authors. Published by WILEY-VCH Verlag GmbH & Co. KGaA, Weinheim. This is an open access article under the terms of the Creative Commons Attribution License, which permits use, distribution and reproduction in any medium, provided the original work is properly cited.

DOI: 10.1002/adfm.201801808

perovskite, e.g., recombination via trap states, can also influence device photovoltage in parallel with interfacial losses. For example, passivation of defects in bulk perovskites has resulted in further enhancement of the PCE of inverted architecture cells, where PCEs > 21% and  $V_{oc}$  > 1.1 V are achieved.<sup>[20]</sup> Spectroscopic studies have revealed that charge carrier trapping processes are significant in solution-processed perovskite thin films,<sup>[21–23]</sup> with these trap states thought to have shallow tail of energies.<sup>[24]</sup> A continuum of energy levels has been observed with such traps state mediating nonradiative recombination, indicating their possible nature as shallow trap states.<sup>[25]</sup> Although a general relationship between a reduction in the concentration of shallow trap states and an improvement in device PCEs has been suggested,<sup>[26–28]</sup> the interplay between bulk perovskite properties, carrier trapping, and photovoltage losses in perovskite solar cells remains unclear. In particular an in situ investigation of such solar cells under operational conditions is required to understand how these shallow traps limit the attainable  $V_{oc}$  in perovskite solar cells.

Previous studies have shown the  $V_{oc}$  to be affected by active layer morphology and composition<sup>[23,29,30]</sup> and charge transport layers.<sup>[16]</sup> Here, we aim to probe the origin of  $V_{oc}$  enhancements and examine the correlation between methylammonium lead triiodide ( $\text{CH}_3\text{NH}_3\text{PbI}_3$ , MAPI) crystallinity, device  $V_{oc}$ , active layer tail states, and charge carrier recombination dynamics using inverted architecture perovskite solar cells. We show that MAPI crystallinity can be tailored by tuning the ratio of precursors in solution, resulting in improvements in the crystallinity of our thin film MAPI layers that significantly reduce  $V_{oc}$  losses. Combining differential charging (DC) and transient photovoltage (TPV) measurements of PSCs under operational conditions, we observe accumulation of photogenerated charge carriers with an exponential distribution versus voltage, we then estimate the corresponding recombination time constant of this charge. Up to an eightfold increase of tail state density is found to correlate with the  $V_{oc}$  losses, these trap states appear to be shallow, and accelerate the recombination rate. Photoluminescence (PL) measurements of the films showed rapid relaxation of carriers and an increased fraction of nonradiative recombination in the presence of higher concentration of trap states.

## 2. Results

Our standard MAPI active layers were prepared from stoichiometric, i.e. 1:1, molar ratios of  $\text{PbI}_2$  and  $\text{CH}_3\text{NH}_3\text{I}$  (methylammonium iodide, MAI). MAPI films with modulated crystallinity were prepared with solutions using excess (+2.5, +5, and +10 mol%) or deficient (–5 mol%) MAI. Note that whenever the terms “MAI excess” or “MAI deficient” are used in this paper, they refer to the relative stoichiometry of the precursor solution, not necessarily the stoichiometry of the resulting perovskite films that was not measured directly. The solution processing of MAPI followed the established “antisolvent dripping” using toluene,<sup>[31]</sup> illustrated schematically in Figure S1 (Supporting Information), with full details in the Experimental Section. In Figure 1a, typical X-ray diffraction (XRD) patterns for the stoichiometric and modified films are shown. All of these data show well-defined diffraction peaks that are assigned to the tetragonal MAPI crystalline phase (and indium-doped tin oxide (ITO) substrate). Figure 1b

shows the calculated integrated peak areas of the (110), (112), and (211) diffraction peaks as a function of excess MAI content in the precursor solution. The (110) peak area increases significantly from MAI-deficient films to MAI-excess films, accompanied by a modest decrease of (112) and (211) peak area. Scanning electron microscopy (SEM) images, Figure 1c–g, show polycrystalline grains that provide continuous substrate coverage of the MAPI films prepared from all solutions. For films prepared over the range from –5% to +5% excess MAI, the SEM images show minimal variation in the thin film morphology, with lateral grain sizes in the region of 150–200 nm. A change of morphology in the MAPI film with 10% excess MAI can be seen in Figure 1g, where grains are less defined in comparison with all other compositions studied, a feature we attribute to excess MAI accumulating in the grain boundaries and surface of the film. Over the range of –5% to 5% excess MAI, there is no evidence of secondary phase formation, e.g.,  $\text{PbI}_2$  or MAI in either the XRD or SEM images.<sup>[32]</sup> Thus, given the comparable morphologies and grain sizes observed – and the comparable film thicknesses, we conclude that the increased intensity of the MAPI {110} diffraction peaks as a distinct improvement in crystallinity with the emergence of a preferential orientation (texture) in the [110] direction. Therefore, in this preparation, the impact of adding excess MAI in the precursor solution is to promote the crystallization and oriented growth of the MAPI. In Table S1 (Supporting Information), we provide the peak positions of the diffraction peaks observed, no discernable change in position is seen with varying the MAI concentration. We would anticipate that if the MAI was uptaken into the perovskite lattice, the resultant defects would cause changes of lattice parameter, the magnitude of which would be within the detection limits of XRD.<sup>[33,34]</sup> We observe a large increase of measured full width at half maximum (FWHM) in the 10% MAI excess film, suggesting a reduction of crystallite size, possibly due to the morphological disruption, shown by the SEM images. In the case where the MAI concentration is substoichiometric the improvements in crystallinity and the emergence of texture are not observed. This may be due to  $\text{PbI}_2$  formation prior to MAPI conversion, i.e., after dripping the antisolvent.<sup>[31]</sup> In contrast, an excess of free methylammonium and iodide ions could accelerate their interaction with  $\text{PbI}_2$  and facilitate full conversion of  $\text{PbI}_2$  into MAPI, schematically shown in Figure S1 (Supporting Information).

Figure 2a shows the current density–voltage ( $J$ – $V$ ) curves of the optimum devices from each processing condition. PEDOT:PSS was used as a hole transport layer, [6,6]-phenyl- $\text{C}_{61}$ -butyric acid methyl ester (PCBM) as an electron transport layer with devices deposited onto ITO-coated glass electrodes and completed with a thermally evaporated LiF/Ag cathode. In Figure 2b, a schematic illustration of the device structures is shown. Photovoltaic parameters, based on 5 pixels, are summarized in Table 1. For the reference device, i.e., 1:1 molar ratio of  $\text{PbI}_2$  and MAI, typical  $V_{oc}$  and PCE values of 0.89 V and 13.7%, respectively, are comparable with literature reports,<sup>[35]</sup> although in general, the performance of such devices is inferior to those prepared in the regular, i.e., noninverted architecture.<sup>[36]</sup> We observe that the device performances show a strong dependence on the crystallinity of MAPI layer and the best device, comprising highly crystalline MAPI prepared with 5% MAI excess, shows a PCE of 16.7% that is comparable with the best

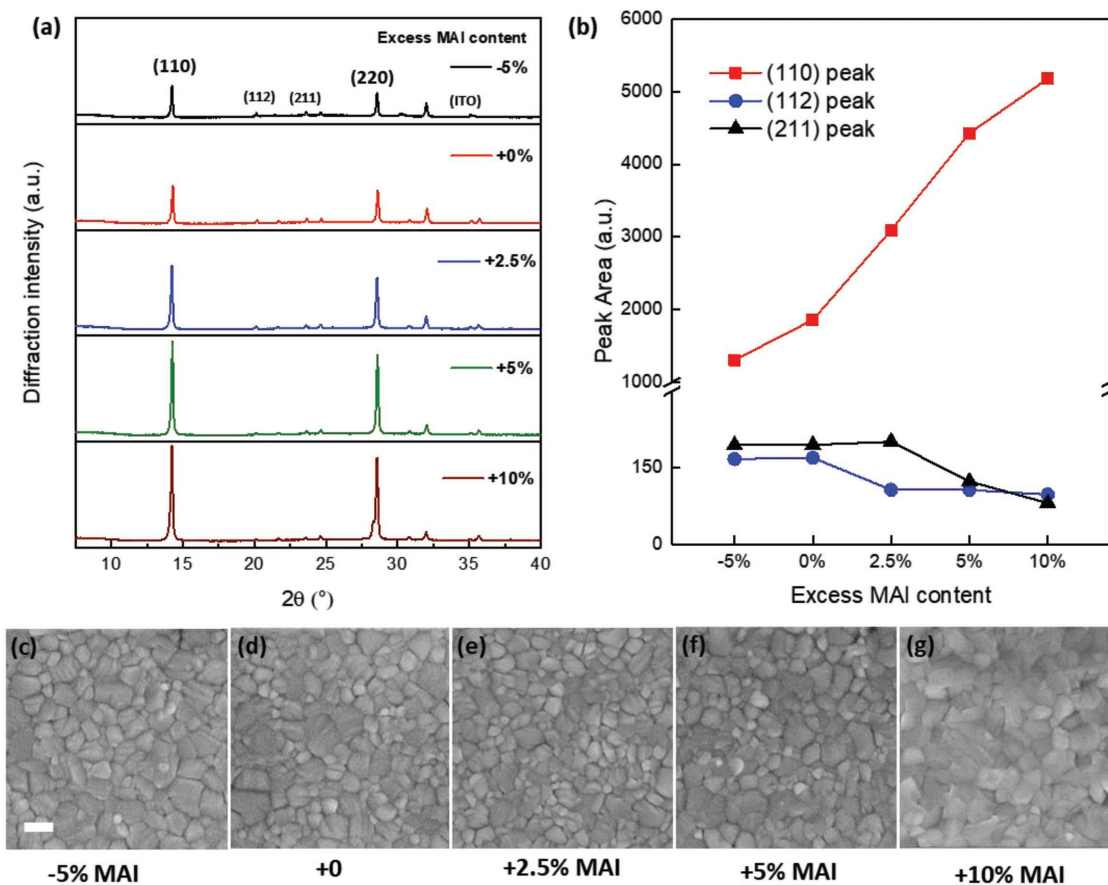


**Figure 1.** a) X-ray diffraction patterns of  $\text{CH}_3\text{NH}_3\text{PbI}_3$  (MAPI) films prepared with solutions containing varying methylammonium iodide (MAI), -5, +0, +2.5, +5, and +10 mol%. b) Measured integrated area of the (110), (112), and (211) diffraction peaks as a function of excess MAI content. c–g) Scanning electron microscopy (SEM) images showing the surfaces of the MAPI films prepared.

efficiencies achieved with this structure in other studies.<sup>[37]</sup> It is apparent from these results that the improvements in  $V_{\text{OC}}$ ,  $\approx 200$  mV, dominate the variation in measured PCE. Importantly, the MAPI films prepared show negligible variation in their optical absorption onset ( $\approx 784$ – $786$  nm for all films), as

confirmed by the absorption spectra in Figure 2b. Additionally, none of the cells (from -5% to 5% MAI) show significant  $J$ - $V$  hysteresis under the measured conditions (Figure S2, Supporting Information). Table 1 also highlights the poor performance of the devices prepared with 10% MAI excess, in such

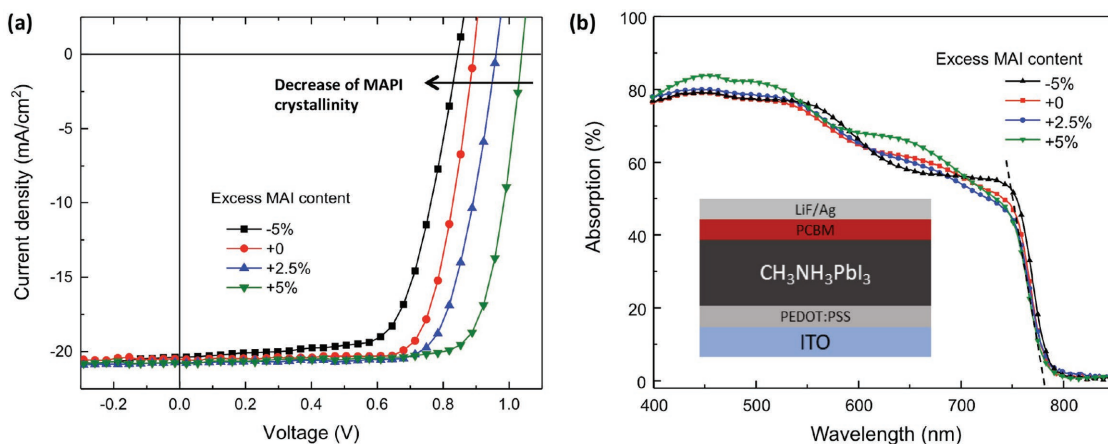


**Figure 2.** a) Current density-voltage ( $J$ - $V$ ) characteristics under AM1.5 1 sun equivalent illumination of MAPI solar cells prepared with a range of MAI concentrations. b) Absorption spectra of the MAPI layers, inset Figure shows the schematic device structure.

**Table 1.** Typical device parameters from solar cells with MAPI prepared by varying MAI:PbI<sub>2</sub> ratios, measured from a minimum of 5 pixels for each processing condition.

Excess MAI content [% <sub>mol</sub> ]	$J_{sc}$ (mA cm <sup>-2</sup> )	$V_{oc}$ (V)	FF	PCE (%)
-5	20.3 ± 0.5	0.844 ± 0.009	0.69 ± 0.01	11.6 ± 0.5
+0	20.5 ± 0.4	0.892 ± 0.006	0.75 ± 0.01	13.7 ± 0.3
+2.5	20.8 ± 0.7	0.960 ± 0.004	0.75 ± 0.01	15.0 ± 0.4
+5	20.8 ± 0.5	1.040 ± 0.008	0.77 ± 0.01	16.7 ± 0.3
+10	18.5 ± 1.2	0.942 ± 0.007	0.71 ± 0.02	12.3 ± 0.6

devices a reduction in  $V_{oc}$ ,  $J_{sc}$ , and fill factor (FF) are observed in addition to the observation of  $J-V$  hysteresis,<sup>[38]</sup> Figure S3 (Supporting Information). This is likely to result from a significant increase in the fraction of recombination via the interfaces in this device,<sup>[10]</sup> a process necessary to observe hysteresis in these devices. Owing to this, we do not consider the 10% MAI-excess films in the following discussions.

To understand the relationship between gains in  $V_{oc}$  and improved MAPI crystallinity, we employed transient optoelectronic measurements to investigate the impact of charge carrier energetics and carrier recombination kinetics on device performance. These techniques have been used to characterize dye-sensitized solar cells,<sup>[39]</sup> organic solar cells,<sup>[40]</sup> and more recently employed to study  $V_{oc}$  losses in perovskite solar cells.<sup>[18,41]</sup> Herein, a DC method is used to estimate capacitance ( $C_{DC}$ ) of operational solar cells, and thus the density of photogenerated charge stored in the cell at equilibrium,  $Q(V_{oc})$ .<sup>[41]</sup> The method combines transient photocurrent measurements with TPV measurements, which are also used to probe charge carrier recombination lifetime ( $\tau_n$ ) at standard device operating conditions. Full details of these measurements can be found in the Experimental Section.

Briefly, a small, pulsed optical perturbation is applied to devices held at a range of  $V_{oc}$  values, achieved by tuning the intensity of constant background illumination from  $\approx 0.01$  to 6 sun equivalent. A small amount of excess charge,  $\Delta Q$ , is created in the devices as a result of the pulsed perturbation, we then probe the resulting voltage change (TPV)  $\Delta V$  ( $\ll V_{oc}$ ) and calculate the differential capacitance as

$$C_{DC}(V) = \frac{\Delta Q}{\Delta V} \quad (1)$$

where in this case,  $V$  corresponds to the steady state  $V_{oc}$  (quasi-Fermi level splitting) resulting from a particular background light intensity. The excess charge  $\Delta Q$  is separately measured with the device held at short circuit by integrating the transient photocurrent (TPC) generated by the same optical perturbation shown in Figure S4 (Supporting Information). The approach assumes that the internal quantum efficiency is close to unity and that the charge generation efficiency of the pulse at short circuit is equivalent to that at open circuit. Typically,  $\Delta Q$  measured at lower light intensities is independent of light intensity, suggesting that recombination loss is negligible during charge extraction, shown in Figure S5 (Supporting Information), and thus can be a correct estimation of  $\Delta Q$  at open circuit for these devices. This small-perturbation approach appears to give a

measure of the capacitance of the electronic charge stored in the device rather than capacitance due to the redistribution of any slow-moving charge (such as that associated with ionic defects).<sup>[41]</sup> As illustrated in Figure 3a,  $C_{DC}$  ( $V = 0$ ), i.e., in the dark, of the measured devices are between 35 and 41 nF cm<sup>-2</sup>. We refer to this capacitance, as determined with no bias light, as the electrode capacitance ( $C_{electrode}$ ) where charge carriers are accumulated at the ITO and Ag contacts. In our previous studies, this electrode capacitance has been shown to be independent of the device  $V_{oc}$  at very low light intensities (and thus low  $V_{oc}$ ),<sup>[18]</sup> corresponding to the horizontal baseline representing  $C_{electrode}$  drawn from  $\approx 0-0.7$  V in Figure 3a. At higher illumination intensities,  $C_{DC}$  is observed to increase exponentially with  $V_{oc}$ , and the exponentially increasing component dominates the overall capacitance for  $>0.2$  sun equivalent. Previously, we assigned this exponential capacitance to the chemical capacitance of MAPI active layer,<sup>[18]</sup> although we note that it could also be related to the accumulation of charge in states at interface regions between the MAPI and charge transport layers.

Fitting the capacitance distribution with an exponential, the total excess electronic charge,  $Q$  [C cm<sup>-2</sup>], stored in the device at open circuit can be estimated by integration of the capacitance with respect to voltage after subtracting  $C_{electrode}$ .

$$Q(V_{oc}) = \int_0^{V_{oc}} C_{DC}(V) - C_{electrode} dV \quad (2)$$

$Q$  is plotted as a function of  $V_{oc}$  corresponding to a range of light intensities in Figure 3b. This exponentially increasing excess electronic charge can be fitted to

$$Q = Q_0 \exp\left(\frac{qV_{oc}}{mk_B T}\right) \quad (3)$$

where  $k_B$  is the Boltzmann constant,  $q$  is the unit charge,  $T$  is the absolute temperature,  $Q_0$  and  $m$  are fitting constants describing the slope and magnitude of the distribution. The exponential relationship of  $Q$  versus  $V_{oc}$  observed at higher light intensities, where  $m \approx 3$ , suggests that at least one charge carrier species may be accumulating in trap states within the MAPI layer or its interfaces since values of  $m > 2$  cannot easily be explained by free charge carriers obeying Boltzmann statistics – particularly in devices where internal variations in electrostatic potential are screened by mobile ionic charge. If this is the case, then the density and distribution of these tail states are parameterized by  $Q_0$  and  $m$ , respectively, in Equation (3).

The significant observation in Figure 3b is that there is a parallel upward shift in the  $Q$  versus  $V_{oc}$  distribution correlated with reduced MAPI crystallinity, manifested in Equation (3) as an increase of  $Q_0$  value (see Table S2 in the Supporting Information). Changes in the distribution of accumulated charge as a function of voltage have previously been observed, and were attributed to the change in the perovskite bandgap resulting from iodide/bromide exchange,<sup>[18]</sup> a temporary redistribution of mobile ionic charge in the perovskite layer,<sup>[41]</sup> or, in organic solar cells, a broadening of density of states.<sup>[42-44]</sup> As there is negligible change of bandgap, minimal hysteresis is in our devices under this measurement regime, and only a limited change is in the slope of the  $Q-V_{oc}$  plot ( $m$  value), the almost parallel shift

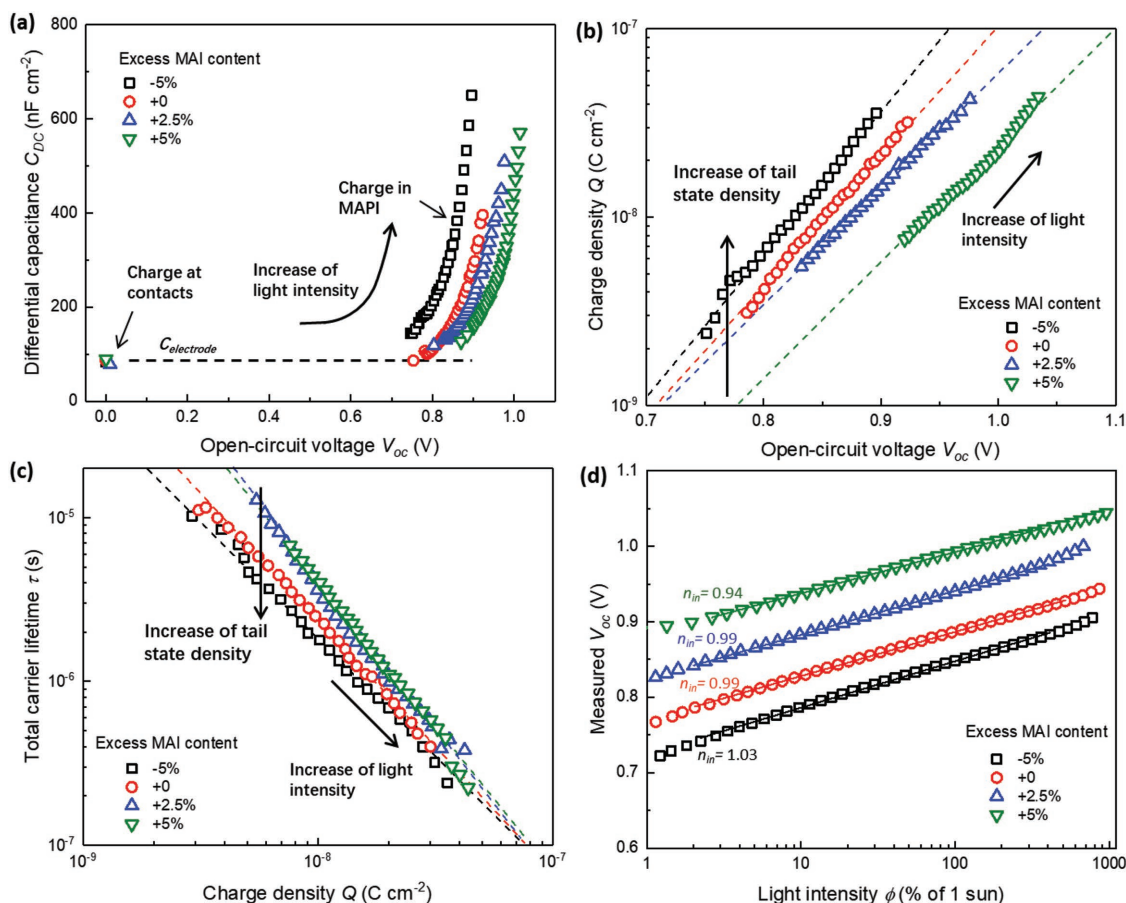


**Figure 3.** a) Differential capacitance ( $C_{DC}$ ) as a function of open-circuit voltage  $V_{oc}$  of solar cells comprising MAPI layers prepared with excess MAI contents of -5, +0, +2.5, and +5 mol% ( $C_{electrode}$  is the electrode capacitance). b) Charge density ( $Q$ ) in the MAPI layers as a function of  $V_{oc}$ . c) Total charge carrier lifetime ( $\tau_n$ ) in the various MAPI devices plotted against  $Q$ . d) Measured  $V_{oc}$  as a function of light intensity and ideality factor obtained from a general fitting of  $V_{oc}$  versus light intensity.

in the  $Q$  versus  $V_{oc}$  relationship could be interpreted either as i) a change in the density of charge stored in subgap tail states or interface states for given quasi-Fermi level splitting ( $V_{oc}$ ), and/or ii) a change in the relative charge carrier energetics, such that for a given amount of accumulated charge, there is a change in the quasi-Fermi level ( $V_{oc}$ ) splitting. For example, in the case of i) when  $V_{oc} = 0.9$  V, the electronic charge in the MAPI layer (+5% excess MAI) will be  $\approx 4.6 \times 10^{-9}$  C cm<sup>-3</sup>, this increases for the same  $V_{oc}$  to  $1.4 \times 10^{-8}$  C cm<sup>-2</sup> (+2.5% MAI),  $2.1 \times 10^{-8}$  C cm<sup>-2</sup> (+0% MAI), and  $3.6 \times 10^{-8}$  C cm<sup>-2</sup> (-5% MAI), i.e., a near eightfold increase in stored charge carriers is required to achieve the same  $V_{oc}$  as a result of an increasing density of tail states. We note that much of this charge may be re-injected/retrapped into the valence/conduction bands from these shallow states multiple times before undergoing recombination.  $Q_0$  describes the magnitude of this distribution of charge trapping states. With this tail density interpretation, there appears to be an eightfold increase of tail state density between +5% and -5% MAI cells. Alternatively, in case ii), for a fixed value of  $Q = 2.1 \times 10^{-8}$  C cm<sup>-2</sup>, the device's  $V_{oc}$  shifts from 0.99 V (+5% MAI), to 0.92 V (+2.5% MAI), 0.89 V (+0% MAI), and to 0.86 V (-5% MAI), which could correspond to the different energetic depths of the tail states where these charge carriers reside.

We consider the change in charge carrier lifetime induced by an increase in subgap tail state density, bearing in mind that charge generation flux is equal but opposite to recombination flux in a working solar cell at open circuit. A relaxation time constant,  $\tau$ , can be derived from decays of TPV transients that is determined by the recombination rate of the photoexcited charge carriers.<sup>[45]</sup> We note herein that TPV lifetimes describe an overall rate of disappearance of photoexcited carriers through recombination in the whole device. These lifetimes, however, may be governed by multiple processes that dominate electrons meeting holes, such as reinjection of carriers from transport layers at lower light intensities.<sup>[46]</sup> Importantly, these transients all demonstrate monoexponential decays, Figure S6 (Supporting Information), reducing the potential complexity of interpreting decays with non-single exponential shapes.<sup>[47]</sup> The small-perturbation lifetime  $\tau$  needs to be converted to the pseudo-first-order lifetime of total excess charge carriers  $\tau_n = \delta\tau$ , by a reaction order of  $\delta$  to estimate recombination flux. The details of this conversion and the comparison of TPV lifetime are discussed in ref. [45]. Both  $\tau$  and  $\tau_n$  are plotted against  $V_{oc}$  in Figure S7 (Supporting Information) with the corresponding values of  $\delta$ . The dependence of  $\tau_n$  on  $Q$ , shown in Figure 3c, demonstrates an approximate power-law correlation for all devices.

$$\tau_n = \tau_{n,0} \left( \frac{Q}{Q_0} \right)^{1-\delta} \quad (4)$$

where  $\tau_{n,0}$ ,  $d$ , and  $Q_0$  are fitting constants. We observe that, for fixed charge density, there is a modest increase (by up to a factor of  $\approx 3$ ) in the total carrier lifetime as the crystallinity of the devices increases, this suggests that less crystalline MAPI not only increases the density trap states, but also accelerates the rate charge carrier recombination via these traps. For example, at  $Q = 2.1 \times 10^{-8} \text{ C cm}^{-2}$ ,  $\tau_n$  for these devices are 1.03  $\mu\text{s}$  (+5% MAI), 0.99  $\mu\text{s}$  (+2.5% MAI), 0.73  $\mu\text{s}$  (0%), and 0.63  $\mu\text{s}$  (−5%). This decrease in lifetime results in minor ( $\approx 25\%$ ) decrease in the amount of accumulated charged in the device at 1 sun illumination. However,  $\tau_n$  versus  $Q$  correlations show minimal change between +2.5% and +5% MAI, indicating that the recombination lifetime is no longer increased by further improvement of crystallinity and may be limited by other processes.

A question arising from examination of the measured lifetimes is that given recombination time constants on the order of 1  $\mu\text{s}$ , which is long by solid state standards, why do we not observe  $V_{oc}$  values approaching 1.2 V.<sup>[2]</sup> The  $V_{oc}$  values we have observed despite comparatively long lifetimes are likely to be related to the capacitive role of the shallow traps that we suggest are present in the device. Although our evidence suggests that recombination via these trap states becomes nontrivial, particularly in the less crystalline examples, the total rate of recombination is still likely to be dominated by the interfaces. Thus, the exchange of charge between these trap states and the free conduction states can explain the comparatively slow recombination kinetics observed. As well as some direct contribution to recombination, the slow capacitive discharge from the traps (related to the idea highlighted by Kiermasch et al.<sup>[46]</sup> where the capacitive discharge is from the contacts) will also effectively slow the rate that charges reach interfaces of the device where the majority of recombination occurs.

The measured stabilized  $V_{oc}$  is plotted against light intensity in Figure 3d, the enhancement in  $V_{oc}$  with increasing MAPI crystallinity is evident. The measurements of excess charge accumulated in the device coupled with the measured photovoltage decay time constants ( $\tau$ ) can be used to reconstruct the measured  $V_{oc}$  to check internal consistency between the measurements (Figure 3d). If we have correctly estimated the amount excess charge accumulated in the working device ( $Q$ ), and the measured photovoltage decay time constants ( $\tau$ ) are related to a recombination process, then we should be able to calculate device  $V_{oc}$  using only these measured data and their corresponding fitting parameters. At open circuit, the recombination flux will equal the flux of generated charge,  $J_{rec} = J_{gen}$ .  $J_{rec}$  is described with the measured charge density  $Q$  and the total recombination lifetime  $\tau_n$  for this quantity of charge.

$$J_{rec} = -\frac{Q}{\tau_n} \quad (5)$$

$J_{gen}$  can be estimated by the short-circuit current density  $J_{sc}$  at each light intensity, shown in Figure S8 (Supporting Information), assuming that there are no significant charge collection losses

at short circuit in these devices. The reconstructed open-circuit voltage,  $V_{oc}^{Rec}$ , can be found by combining Equations (3)–(5).

$$V_{oc}^{Rec} = \frac{mk_B T}{q\delta} \ln \left( \frac{\tau_{n,0} J_{sc}}{Q_0} \right) \quad (6)$$

The fitting parameters  $m$ ,  $\delta$ ,  $\tau_{n,0}$ ,  $Q_0$  are listed in Table S2 (Supporting Information), and the derived values of  $V_{oc}^{Rec}$  are consistent with the original measured values of  $V_{oc}$ , shown in Figure S9 (Supporting Information).

Equation (6) also enables determination of the dependence of the  $V_{oc}$  on light intensity. Considering that we observe an approximately linear dependence, at least at 0.1–3 sun equivalent, between the short-circuit photocurrent and light intensity (Figure S6, Supporting Information), and again assuming collection losses are small, we can use  $J_{sc}$  as a proxy for the light intensity. By differentiating Equation (6) with respect to  $\ln(J_{sc})$ , we arrive at an expression for the steady state cell ideality factor.

$$n_{id} = \frac{\delta}{m} = \frac{q}{k_B T} \cdot \frac{dV_{oc}}{d \ln(J_{sc})} \quad (7)$$

The ideality factor  $n_{id}$  can thus be obtained by fitting the  $V_{oc}$  versus light intensity relationship, labeled in Figure 3d, where it is apparent the values are close to unity for all devices. The ideality factor is also evaluated and plotted as a function of light intensity in Figure S10 (Supporting Information), confirming this observation up to  $\approx 3$  sun equivalent light intensity, the deviation at higher light intensities is likely to be primarily due to an increase in the cell temperature which was not corrected for. Assuming that the recombination processes observed in this study are primarily mediated by trap states, a value of  $n_{id} \approx 1$  suggests that trap states either in the bulk or at the interfaces are energetically shallow relative to the conduction/valence bands,<sup>[48]</sup> it is also consistent with the strong interfacial recombination observed in devices with PEDOT:PSS contacts.<sup>[49]</sup>

To explore further the nature of the electronic states within active layers, we characterized the charge carrier recombination in a reference MAPI film (1:1 ratio of MAI and  $\text{PbI}_2$ ) film and the best-performing MAPI film (+5% MAI), with PL spectroscopy. Steady-state PL spectra of active layer films are plotted in Figure 4a, these show that the emission intensity is about 15 times greater in the +5% MAI film than in the reference. The substantial increase of PL intensity strongly suggests a reduction in nonradiative Shockley–Read–Hall recombination processes, and the density of trap states in the MAPI film is largely reduced. The recombination dynamics of the two films are shown by the time-resolved PL (TRPL) decays in Figure 4b, measured with time-correlated single-photon counting (TCSPC) and probed at peak position of PL emission spectra. The decays of both films are clearly biphasic, with a fast (nanosecond) initial decay followed by a slower ( $\approx 100$  ns) decay. The biphasic features in PL decay dynamics have been intensively reported and studied for solution-processed perovskite films,<sup>[21,22,50,51]</sup> where the fast phase is assigned to charge carriers trapping into the nonradiative trap states, and the slow phase assigned to subsequent recombination processes of the remaining carrier population. Here, decay dynamics for the reference, lower crystallinity film are faster compared to the +5% MAI excess

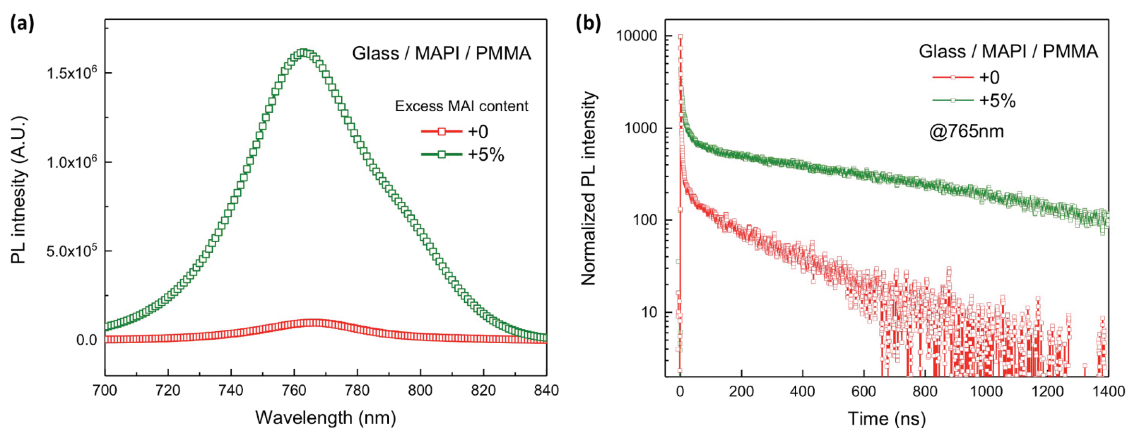


**Figure 4.** a) Steady state photoluminescence (PL) emission spectra of MAPI films prepared with stoichiometric  $\text{PbI}_2$ :MAI and +5 mol% MAI. b) Time-resolved PL decay spectra probed at 765 nm where the stoichiometric MAPI film shows much larger amplitude of initial fast decay.

film (biexponential decay times of 1.4 and 370 ns compared to 2.7 and 735 ns, respectively), these differences in carrier recombination lifetimes are roughly consistent with the relative difference in TPV transients for the devices. More importantly, at the lower crystallinity, reference MAPI films show a much larger amplitude of fast decay phase, suggesting that a larger fraction of the initial population of photogenerated charge carriers are trapped, consistent with the higher  $Q_0$  derived from the data in Figure 3b. PL emission spectra of the MAPI films in contact with either the ETL and HTL are shown in Figure S11 (Supporting Information). The results show that the addition of a PCBM layer to the 1:1 film only quenches the PL by a factor of  $\approx 4$  compared to  $>40\times$  for the 5% MAI excess film, indicating poor electron collection efficiency by the PCBM in the presence of the trap states. Conversely, holes are collected at the PEDOT:PSS contact with a relatively higher efficiency than the electrons in the 1:1 film  $\approx 40\times$ . Thus, it suggests that electrons are the species primarily affected by shallow trap states.<sup>[24]</sup> A nontrivial fraction of the recombination will also occur by re-emission of charge back into the active layer or interface states following collection at the contacts.<sup>[46]</sup> The PL quenching measurements also indicate an overall higher radiative yield from the quenched +5% MAI films relative to the quenched 1:1 films ( $\approx 1.5$  times for MAPI/PCBM and  $\approx 5$  times for the MAPI/PEDOT:PSS). This is consistent with observations in Figure 4 for the unquenched films, indicating an overall higher probability that carriers will recombine radiatively in the low trap density films regardless of whether they can be collected at a contact, showing that reduction in trap-mediated recombination also prevails in the heterojunction interfaces as a substantial process to reduce  $V_{oc}$  loss.

### 3. Discussion

Trap-mediated recombination in solution-processed MAPI has been well studied, both with spectroscopy and microscopy.<sup>[51–54]</sup> Here, we have provided an insight into how these nonradiative losses in bulk MAPI can limit device  $V_{oc}$ . The observation of  $Q$  versus  $V_{oc}$  relationships in Figure 3a implies that at least one type of charge carrier is stored in an exponential of subgap

states in the active layer or its interfaces. Figure 5a schematically describes this difference in a flat-band energy diagram. The increase in the trap density in the less crystalline films also mediates recombination somewhat more rapidly at the expense of radiative pathways. Combined with our observation of device ideality close to unity, these electronic traps appear to be energetically shallow, which is consistent with the literature.<sup>[24,51]</sup> Figure 5b schematically depicts the recombination of charge carriers via tail states, where photogenerated charge carriers are first trapped into the tail states, from which they may either detrapp or nonradiatively recombine. We note that the variation in recombination time constant for a given photoinduced charge concentration might also be correlated with a change in the majority species carrier concentration in the MAPI. For some MAPI preparations, excess MAI, as well as improved crystallinity through annealing, has been shown to result in a reduction in the free electron concentration, making the material more intrinsic,<sup>[55,56]</sup> which we would expect to increase the free carrier lifetime. However, if this were the only effect induced by MAI, then we would not expect the PL efficiency to be as sensitive to MAI fraction as observed in Figure 4.

Recently Kiermasch et al. have reminded the community that the release of capacitively accumulated free charges can prolong the time constants observed in TPV measurements.<sup>[46]</sup> Their study raises the possibility that the charge distribution we have observed in these devices is not accumulated within traps but simply corresponds to free charge within the active layer or contacts. We note that TPV time constants may also be prolonged by the same mechanism of capacitive storage and release of charge from trap states – an effect well documented for dye sensitized solar cells,<sup>[39]</sup> and also suggested to explain recombination rates in organic bulk heterojunction films without electrical contacts.<sup>[57]</sup> Although we cannot definitively rule out the possibility that the  $Q$  versus  $V_{oc}$  distribution we have measured arise from a capacitive accumulation of free charges, the following factors make it an unlikely explanation for our observations. We observe  $Q$  versus  $V_{oc}$  slopes of  $m \approx 3$  but a steady state ideality factor of  $n_{id} = 1$ . In a perovskite device, if only free charges were present, we would expect  $m = n_{id}$  when measured at steady state if no trapped charge is present.<sup>[48]</sup> A value of  $m > 2$  cannot easily be explained by

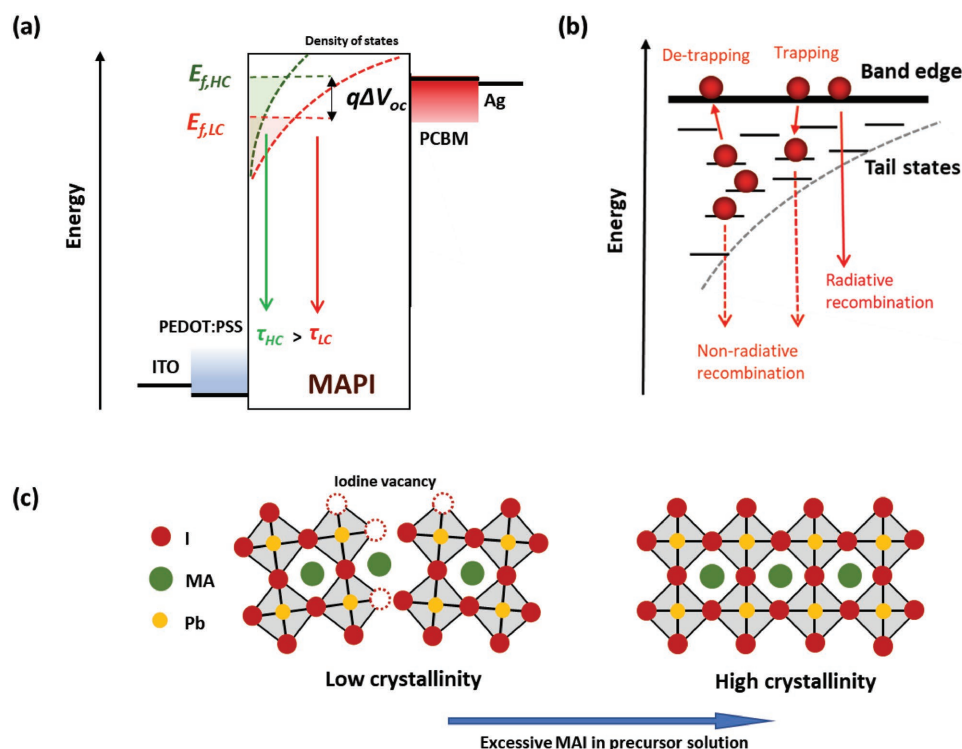


**Figure 5.** a) Schematic illustration of increased tail state density in a flat-band energy diagram of a perovskite solar cell, with high-crystallinity (HC) and low-crystallinity (LC) MAPI, and with their corresponding electron quasi-Fermi levels,  $E_{f,HC}$  and  $E_{f,LC}$ , and charge carrier recombination lifetimes,  $\tau_{HC}$  and  $\tau_{LC}$ .  $\Delta V_{oc}$  is the  $V_{oc}$  loss due to increased tail state density. b) Schematic depiction of charge carrier recombination via tail states, including charge trapping (also with detrapping), nonradiative recombination from the tail states, a radiative recombination from band edges. c) Schematic illustration indicating the improvement in MAPI crystallinity.

free charge carriers obeying Boltzmann statistics, particularly in devices where internal variations in electrostatic potential are screened by mobile ionic charge. Thus, the value of  $m \approx 3$ , coupled with our PL observations, appears consistent with a shallow distribution of trap states.

This work addresses nonradiative losses which are likely to originate in the bulk of the perovskite, the  $V_{oc}$  (1.04 V) and PCE (16.6%) achieved with our best cells are lower than the best reported device performances using similar perovskite absorbers cf.  $V_{oc} > 1.1$  V, PCE  $\approx 20\%$ . This is mainly attributed to our use of PEDOT:PSS as the HTL, which is associated with significant interfacial recombination,<sup>[11,49]</sup> compared with  $TiO_2$ -based conventional cells or inverted cells employing alternative HTLs.<sup>[35,36]</sup> We observed in Figure 3c that total charge carrier lifetime as a function of charge concentration is not significantly altered with a change in MAPI crystallinity from +2.5% to +5% MAI, which may imply that interfacial recombination, either at PEDOT:PSS/MAPI or MAPI/PCBM interfaces became the limiting factor of carrier lifetime and thus the recombination flux in the whole device. Further increases of  $V_{oc}$  and PCE can be achieved by suppressing the interfacial recombination.<sup>[3,58]</sup> Thus, we may theorize that reducing nonradiative losses in bulk perovskite and at interfaces are two parallel methods toward high  $V_{oc}$  of perovskite solar cells.

We find an increased density of tail states and increased nonradiative recombination are associated with reduced crystallinity of MAPI. Trap states are likely to be localized at crystallite surfaces or interfaces due to a break of bulk crystallite

symmetry,<sup>[53]</sup> but additionally, PL quenching is correlated with the presence of lattice defects, e.g., halide vacancies.<sup>[59,60]</sup> The observed increase of X-ray diffraction intensity of MAPI films, seen in Figure 1a,b should describe an extension of order in the MAPI, and/or filling of lattice vacancies, which is schematically shown in Figure 5c. In this study, improved MAPI crystallinity was achieved using the MAI-rich precursor solutions during processing, although we note that a MAI excess appears to increase trap densities using different fabrication protocols.<sup>[61]</sup> Mixed-cation lead mixed-halide perovskites have now surpassed conventional MAPI perovskites with reported PCE exceeding 20%,<sup>[6,20]</sup> the optoelectronic properties and phase stability of these materials are also highly dependent on crystallinity.<sup>[50,62]</sup> This is entirely consistent with our detailed studies that conclude that improving perovskite crystallinity is a crucial strategy to eliminating trap states.

#### 4. Conclusions

We have identified decrease in MAPI crystallinity as an origin of  $V_{oc}$  losses in perovskite solar cells. We show that MAPI crystallinity can be systematically tailored by tuning the stoichiometry of precursor mix in solution, where excess MAI, up to 5% in the precursor solution, strongly promotes the crystallization of MAPI without detrimental effects. Improved crystallinity of thin-film MAPI results in  $\approx 200$  mV increase in  $V_{oc}$  and a PCE enhancement from 11.3% to 16.7% in inverted solar cells



using PEDOT:PSS as a HTL. With in situ differential charging and transient photovoltage characterization, we show accumulation of photogenerated charge carriers in exponentially distributed subgap tail states. An increase of density of these shallow trap states, associated with reduced MAPI crystallinity, results in accelerated nonradiative recombination rate with a corresponding loss in  $V_{oc}$ . Improving MAPI crystallinity is an essential step on the route to optimizing the performance of solution-processed active layers and devices, with our simple methodology highlighting the impact of facile modifications in processing that have a complex impact on device electronic structure and performance.

## 5. Experimental Section

**Device Fabrication and Measurement:** All devices were fabricated on ITO (Piotec, UK) glass, a transparent conducting substrate. The substrates were sequentially cleaned in ultrasonic bath in acetone, isopropanol, and deionized water for 10 min, respectively, and were dried under argon flow. PEDOT:PSS was spin-coated onto the substrates as electron blocking layer at 3500 rpm for 45 s, and was annealed at 150 °C for 15 min. Prior to spin-coating, all ITO substrates were treated by oxygen plasma for 10 min.

The precursor solution of perovskite was prepared by codissolving 1.2 M lead iodide ( $PbI_2$ , Aldrich) and MAI (Solaronix) in mixed solvent of gamma-butyrolactone and dimethyl sulfoxide (Aldrich, 7:3 by volume). The solution was stirred for 1 h at 60 °C, and was filtered before use. The perovskite active layer was formed via a toluene-dripping method. The precursor solution was first spun at 500 rpm for 5 s and then at 2000 rpm for 20 s. 0.5 mL of toluene was instantly dripped onto the film right at the end of second stage of spinning, and followed by spinning at 4000 rpm for 20 s. The films were transferred onto a hot plate after spin-coating, and were dried at 100 °C for 10 min to crystallize the perovskite.

The ETLs were deposited on perovskite by spin-coating PCBM (18 mg mL<sup>-1</sup> in chlorobenzene) at 1300 rpm for 60 s. Finally, the devices were completed by thermally evaporating 0.7 nm of LiF and 100 nm of Ag onto PCBM under  $5 \times 10^{-6}$  mbar. Except for PEDOT:PSS deposition, all other solution processing was performed inside a nitrogen-filled glovebox.

Current density–voltage ( $J$ – $V$ ) characteristics were measured by applying external potential bias to the cell and recording the current with a Keithley 2400 source meter, with a scanning rate of 50 mV s<sup>-1</sup>. The cells were illuminated by an AM1.5 xenon lamp solar simulator (Oriental Instruments). The intensity was adjusted to 1 sun by changing the working current, which was calibrated using a Si reference photodiode. All devices were stored in dark prior to measurement and were measured in a nitrogen-filled chamber.

**Physical and Structural Characterization:** XRD patterns of perovskite films were obtained with a X'Pert Powder diffractometer (PANalytical), Cu K $\alpha$  source. The diffraction patterns were measured over the range 7°–40° 2 $\theta$ . The perovskite films were measured with ITO/PEDOT:PSS/perovskite/PCBM structure. The samples were rotated during measurement. The top-view SEM images were obtained using a LEO Gemini 1525 field emission gun scanning electron microscopy. The working voltage of SEM was fixed at 5 kV. To prevent charging, all the films were coated with 10 nm Cr layer.

**Photoluminescence Spectroscopy:** For steady state PL (Laserglow Technologies), the sample films were sealed by slide glass with surlyn (Solaronix) and were illuminated with 635 nm monochromatic light (15 mW cm<sup>-2</sup>) and the PL intensity was measured from 700 to 850 nm. All samples were measured 1 day after preparation, the same time length between device preparation and measurement, and were kept under dark before measurement. The PL decay was measured by time-correlated single-photon counting with Horriba spectrofluorometer with 635 nm

excitation. PL quenching efficiency is estimated by difference of emission intensity at peak position with and without contact layer. Ultraviolet–visible (UV–vis) absorption spectra were obtained by measuring both the transmittance and reflectance spectra of the perovskite films, with step size of 1 nm and integrating time of 0.5 s.

**Transient Optoelectronic Measurements:** Differential charging, transient photocurrent (TPV) and transient photovoltage (TPV) were carried out. The background illumination was provided by 12 white light emitting diodes with adjustable power output. The intensity was first calibrated to the  $J_{sc}$  of devices measured under AM1.5 solar simulator. Any changes in background illumination were followed by a delay time of 10 s before commencing TPC or TPV measurements. Small optical perturbation was provided by 532 nm pulsed neodymium-doped yttrium aluminum garnet laser, of which the intensity was fixed during the whole measurement. The devices were in a nitrogen-filled testing chamber to minimize the exposure to oxygen and moisture.

Firstly, full light level calibration was carried out by measuring the device  $V_{oc}$ s as well as  $J_{sc}$ s under a range of illumination intensities (0.5–900% sun), and later the devices were able to be held at different  $V_{oc}$  by tuning the light intensities. Secondly, TPC measurement was performed to determine the small amount of excess charge  $\Delta Q$ . The device was held close to short-circuit condition with a 50  $\Omega$  resistance and was connected with a Tektronix TDS3032 oscilloscope. The resulting photocurrent transient by laser perturbation was integrated with respect to time to obtain an estimation of  $\Delta Q$ . The average value of  $\Delta Q$  was measured at low light (<25%), where the value of  $\Delta Q$  exhibited minimal variation with background light intensity levels (Figure S5, Supporting Information). Thirdly, TPV measurement was done with device holding at open circuit by connecting a 1 M $\Omega$  impedance with the oscilloscope. The small photovoltage transient due to the same laser perturbation with TPC, shown in Figure S6 (Supporting Information), was fitted with a monoexponential decay to obtain the small perturbation carrier lifetime  $\tau_{\Delta n}$ . TPV measurements were carried out between 0.5% sun and 600% of 1 sun equivalent.

## Supporting Information

Supporting Information is available from the Wiley Online Library or from the author.

## Acknowledgements

The authors acknowledge the funding from the Stephen and Ana Hui Fellowship (Imperial College London), the Welsh government Sêr Cymru Solar programme, and the EPSRC projects under Grant Numbers EP/M025020/1, EP/P02484X/1, and EP/M014797/1. Additionally, the authors acknowledge the EPSRC Centre for Doctoral Training in Plastic Electronic Materials EP/L016702/1 for student support and training. The authors are grateful to Dr. Phil Calado (Imperial College London) for useful discussions regarding this work.

## Conflict of Interest

The authors declare no conflict of interest.

## Keywords

crystallinity, open-circuit voltage, perovskite solar cells, tail states

Received: March 12, 2018

Revised: April 29, 2018

Published online: June 25, 2018

- [1] J.-P. Correa-Baena, A. Abate, M. Saliba, W. Tress, T. Jesper Jacobsson, M. Grätzel, A. Hagfeldt, *Energy Environ. Sci.* **2017**, *10*, 710.
- [2] W. Tress, *Adv. Energy Mater.* **2017**, *7*, 1602358.
- [3] J.-P. Correa-Baena, W. Tress, K. Domanski, E. H. Anaraki, S.-H. Turren-Cruz, B. Roose, P. P. Boix, M. Grätzel, M. Saliba, A. Abate, A. Hagfeldt, *Energy Environ. Sci.* **2017**, *10*, 1207.
- [4] J. Yao, T. Kirchartz, M. S. Vezie, M. A. Faist, W. Gong, Z. He, H. Wu, J. Troughton, T. Watson, D. Bryant, J. Nelson, *Phys. Rev. Appl.* **2015**, *4*, 014020.
- [5] S. D. Stranks, *ACS Energy Lett.* **2017**, *2*, 1515.
- [6] M. Saliba, T. Matsui, J.-Y. Seo, K. Domanski, J.-P. Correa-Baena, M. K. Nazeeruddin, S. M. Zakeeruddin, W. Tress, A. Abate, A. Hagfeldt, M. Grätzel, *Energy Environ. Sci.* **2016**, *9*, 1989.
- [7] C. Tao, J. Van Der Velden, L. Cabau, N. F. Montcada, S. Neutzner, A. R. Srimath Kandada, S. Marras, L. Brambilla, M. Tommasini, W. Xu, R. Sorrentino, A. Perinot, M. Caironi, C. Bertarelli, E. Palomares, A. Petrozza, *Adv. Mater.* **2017**, *29*, 1604493.
- [8] J. Seo, S. Park, Y. Chan Kim, N. J. Jeon, J. H. Noh, S. C. Yoon, S. Il Seok, P. S. Cells, *Energy Environ. Sci.* **2014**, *7*, 2642.
- [9] J.-Y. Jeng, Y.-F. Chiang, M.-H. Lee, S.-R. Peng, T.-F. Guo, P. Chen, T.-C. Wen, *Adv. Mater.* **2013**, *25*, 3727.
- [10] P. Calado, A. M. Telford, D. Bryant, X. Li, J. Nelson, B. C. O'Regan, P. R. F. Barnes, *Nat. Commun.* **2016**, *7*, 13831.
- [11] D. Liu, Y. Li, J. Yuan, Q. Hong, G. Shi, D.-X. Yuan, J. Wei, C.-C. Huang, J. Tang, M.-K. Fung, *J. Mater. Chem. A* **2017**, *5*, 5701.
- [12] D. Zhao, M. Sexton, H. Y. Park, G. Baure, J. C. Nino, F. So, *Adv. Energy Mater.* **2015**, *5*, 1.
- [13] C. Bi, Q. Wang, Y. Shao, Y. Yuan, Z. Xiao, J. Huang, *Nat. Commun.* **2015**, *6*, 7747.
- [14] J. H. Park, J. Seo, S. Park, S. S. Shin, Y. C. Kim, N. J. Jeon, H. W. Shin, T. K. Ahn, J. H. Noh, S. C. Yoon, C. S. Hwang, S. Il Seok, *Adv. Mater.* **2015**, *27*, 4013.
- [15] S. Chen, Y. Hou, H. Chen, M. Richter, F. Guo, S. Kahmann, X. Tang, T. Stubhan, H. Zhang, N. Li, N. Gasparini, C. O. R. Quiroz, L. S. Khazada, G. J. Matt, A. Osvet, C. J. Brabec, *Adv. Energy Mater.* **2016**, *6*, 1600132.
- [16] Y. Shao, Y. Yuan, J. Huang, *Nat. Energy* **2016**, *1*, 15001.
- [17] C. M. Wolff, F. Zu, A. Paulke, L. P. Toro, N. Koch, D. Neher, *Adv. Mater.* **2017**, *29*, 1.
- [18] S. Wheeler, D. Bryant, J. Troughton, T. Kirchartz, T. M. Watson, J. Nelson, J. R. Durrant, *J. Phys. Chem. C* **2017**, *121*, 13496.
- [19] H.-S. Kim, I. Mora-Sero, V. Gonzalez-Pedro, F. Fabregat-Santiago, E. J. Juarez-Perez, N.-G. Park, J. Bisquert, *Nat. Commun.* **2013**, *4*, 2242.
- [20] X. Zheng, B. Chen, J. Dai, Y. Fang, Y. Bai, Y. Lin, H. Wei, X. C. Zeng, J. Huang, *Nat. Energy* **2017**, *2*, 17102.
- [21] Y. Yamada, T. Nakamura, M. Endo, A. Wakamiya, Y. Kanemitsu, *J. Am. Chem. Soc.* **2014**, *136*, 11610.
- [22] X. Wen, Y. Feng, S. Huang, F. Huang, Y. Cheng, M. Green, A. Ho-Baillie, *J. Mater. Chem. C* **2015**, *4*, 793.
- [23] S. Shao, M. Abdu-Aguye, T. S. Sherkar, H. Fang, S. Adjokatse, G. ten Brink, B. J. Kooi, L. Koster, M. A. Loi, *Adv. Funct. Mater.* **2016**, *26*, 8094.
- [24] T. Leijtens, G. E. Eperon, A. J. Barker, G. Grancini, W. Zhang, J. M. Ball, A. R. S. Kandada, H. J. Snaith, A. Petrozza, *Energy Environ. Sci.* **2016**, *9*, 3472.
- [25] A. D. Wright, R. L. Milot, G. E. Eperon, H. J. Snaith, M. B. Johnston, L. M. Herz, *Adv. Funct. Mater.* **2017**, *27*, 1700860.
- [26] Y. C. Kim, N. J. Jeon, J. H. Noh, W. S. Yang, J. Seo, J. S. Yun, A. Ho-Baillie, S. Huang, M. A. Green, J. Seidel, T. K. Ahn, S. Il Seok, *Adv. Energy Mater.* **2015**, *6*, 1502104.
- [27] J. You, Y. (Michael) Yang, Z. Hong, T.-B. Song, L. Meng, Y. Liu, C. Jiang, H. Zhou, W.-H. Chang, G. Li, Y. Yang, *Appl. Phys. Lett.* **2014**, *105*, 183902.
- [28] W. Nie, H. Tsai, R. Asadpour, A. J. Neukirch, G. Gupta, J. J. Crochet, M. Chhowalla, S. Tretiak, M. A. Alam, H. Wang, *Science* **2015**, *347*, 522.
- [29] W. Qiu, T. Merckx, M. Jaysankar, C. M. de la Huerta, L. Rakocevic, W. Zhang, U. W. Paetzold, R. Gehlhaar, L. Froyen, J. Poortmans, *Energy Environ. Sci.* **2016**, *9*, 484.
- [30] Y. H. Lee, J. Luo, R. Humphry-Baker, P. Gao, M. Grätzel, M. K. Nazeeruddin, *Adv. Funct. Mater.* **2015**, *25*, 3925.
- [31] N. J. Jeon, J. H. Noh, Y. C. Kim, W. S. Yang, S. Ryu, S. Il Seok, *Nat. Mater.* **2014**, *13*, 897.
- [32] T. Du, C. H. Burgess, J. Kim, J. Zhang, J. R. Durrant, M. A. McLachlan, *Sustainable Energy Fuels* **2017**, *1*, 119.
- [33] R. Maller, Y. Porte, H. N. Alshareef, M. A. McLachlan, *J. Mater. Chem. C* **2016**, *4*, 5953.
- [34] J. B. Franklin, B. Zou, P. Petrov, D. W. McComb, M. P. Ryan, M. A. McLachlan, *J. Mater. Chem.* **2011**, *21*, 8178.
- [35] T. Liu, K. Chen, Q. Hu, R. Zhu, Q. Gong, *Adv. Energy Mater.* **2016**, *6*, 1600457.
- [36] W. Yan, S. Ye, Y. Li, W. Sun, H. Rao, Z. Liu, Z. Bian, C. Huang, *Adv. Energy Mater.* **2016**, *6*, 1600474.
- [37] L. Meng, J. You, T. F. Guo, Y. Yang, *Acc. Chem. Res.* **2016**, *49*, 155.
- [38] H. Yu, H. Lu, F. Xie, S. Zhou, N. Zhao, *Adv. Funct. Mater.* **2016**, *26*, 1411.
- [39] P. R. F. Barnes, K. Miettunen, X. Li, A. Y. Anderson, T. Bessho, M. Gratzel, B. C. O'Regan, *Adv. Mater.* **2013**, *25*, 1881.
- [40] D. Credgington, F. C. Jamieson, B. Walker, T. Q. Nguyen, J. R. Durrant, *Adv. Mater.* **2012**, *24*, 2135.
- [41] B. C. O'Regan, P. R. F. Barnes, X. Li, C. Law, E. Palomares, J. M. Marin-Beloqui, *J. Am. Chem. Soc.* **2015**, *137*, 5087.
- [42] S. D. Collins, C. M. Proctor, N. A. Ran, T.-Q. Nguyen, *Adv. Energy Mater.* **2016**, *6*, 1501721.
- [43] T. Heumueller, T. M. Burke, W. R. Mateker, I. T. Sachs-Quintana, K. Vandewal, C. J. Brabec, M. D. McGehee, *Adv. Energy Mater.* **2015**, *5*, 1500111.
- [44] S. A. Hawks, F. Deledalle, J. Yao, D. G. Rebois, G. Li, J. Nelson, Y. Yang, T. Kirchartz, J. R. Durrant, *Adv. Energy Mater.* **2013**, *3*, 1201.
- [45] C. G. Shuttle, B. O'Regan, A. M. Ballantyne, J. Nelson, D. D. C. Bradley, J. De Mello, J. R. Durrant, *Appl. Phys. Lett.* **2008**, *92*, 90.
- [46] D. Kiermasch, A. Baumann, M. Fischer, V. Dyakonov, K. Tvingstedt, *Energy Environ. Sci.* **2018**, *11*, 629.
- [47] N. F. Montcada, J. M. Marin-Beloqui, W. Cambarau, J. Jiménez-López, L. Cabau, K. T. Cho, M. K. Nazeeruddin, E. Palomares, *ACS Energy Lett.* **2017**, *2*, 182.
- [48] P. Calado, D. Burkitt, J. Yao, J. Troughton, T. M. Watson, M. J. Carnie, A. M. Telford, B. C. O'Regan, J. Nelson, P. R. F. Barnes, *arXiv:1804.09049v1* **2018**.
- [49] W. Tress, M. Yavari, K. Domanski, P. K. Yadav, B. Niesen, J.-P. Correa-Baena, A. Hagfeldt, M. Grätzel, *Energy Environ. Sci.* **2017**, *11*, 151.
- [50] S. D. Stranks, V. M. Burlakov, T. Leijtens, J. M. Ball, A. Goriely, H. J. Snaith, *Phys. Rev. Appl.* **2014**, *2*, 1.
- [51] D. W. deQuilettes, S. M. Vorpahl, S. D. Stranks, H. Nagaoka, G. E. Eperon, M. E. Ziffer, H. J. Snaith, D. S. Ginger, *Science* **2015**, *348*, 683.
- [52] G. J. A. H. Wetzelaer, M. Scheepers, A. M. Sempere, C. Momblona, J. Avila, H. J. Bolink, *Adv. Mater.* **2015**, *27*, 1837.
- [53] X. Wu, M. T. Trinh, D. Niesner, H. Zhu, Z. Norman, J. S. Owen, O. Yaffe, B. J. Kudsich, X. Y. Zhu, *J. Am. Chem. Soc.* **2015**, *137*, 2089.
- [54] M. Yang, Y. Zeng, Z. Li, D. Kim, C.-S. Jiang, J. van de Lagemaat, K. Zhu, *Phys. Chem. Chem. Phys.* **2017**, *19*, 5043.
- [55] Q. Wang, Y. Shao, H. Xie, L. Lyu, X. Liu, Y. Gao, J. Huang, *Appl. Phys. Lett.* **2014**, *105*, 163508.

- [56] C. Bi, Y. Shao, Y. Yuan, Z. Xiao, C. Wang, Y. Gao, J. Huang, *J. Mater. Chem. A* **2014**, *2*, 18508.
- [57] M. P. Eng, P. R. F. Barnes, J. R. Durrant, *J. Phys. Chem. Lett.* **2010**, *1*, 3096.
- [58] Y. Hou, W. Chen, D. Baran, T. Stubhan, N. A. Luechinger, B. Hartmeier, M. Richter, J. Min, S. Chen, C. O. R. Quiroz, N. Li, H. Zhang, T. Heumueller, G. J. Matt, A. Osvet, K. Forberich, Z. G. Zhang, Y. Li, B. Winter, P. Schweizer, E. Spiecker, C. J. Brabec, *Adv. Mater.* **2016**, *28*, 5112.
- [59] D. W. deQuilettes, W. Zhang, V. M. Burlakov, D. J. Graham, T. Leijtens, A. Osheroov, V. Bulović, H. J. Snaith, D. S. Ginger, S. D. Stranks, *Nat. Commun.* **2016**, *7*, 11683.
- [60] E. T. Hoke, D. J. Slotcavage, E. R. Dohner, A. R. Bowering, H. I. Karunadasa, M. D. McGehee, *Chem. Sci.* **2015**, *6*, 613.
- [61] M. L. Petrus, Y. Hu, D. Moia, P. Calado, A. M. A. Leguy, P. R. F. Barnes, P. Docampo, *ChemSusChem* **2016**, *9*, 2699.
- [62] W. Rehman, D. P. McMeekin, J. B. Patel, R. L. Milot, M. B. Johnston, H. J. Snaith, L. M. Herz, *Energy Environ. Sci.* **2017**, *10*, 361.